Research Article

Rapid Joule-heating synthesis of metal/carbon-based electrocatalysts for efficient carbon dioxide reduction

Weijian Guo[#], Xueying Cao[#], Ao Zhou, Wenwen Cai, Jintao Zhang[*]

Key Laboratory for Colloid and Interface Chemistry (Ministry of Education), School of Chemistry and Chemical Engineering, Shandong University, Jinan 250100, China

ARTICLE INFO

ABSTRACT

Carbon-loaded metal nanoparticles (NPs) are widely employed as functional materials for electrocatalysis. In this study, a rapid thermal shock method was developed to load various metal nanoparticles onto carbon supports. Compared to conventional pyrolysis processes, Joule heating enables rapid heating to elevated temperatures within a short period, effectively preventing the migration and aggregation of metal atoms. Simultaneously, the anchoring effect of defective carbon carriers ensures the uniform distribution of NPs on the carbon supports. Additionally, nitrogen doping can significantly enhance the electronic conductivity of the carbon matrix and strengthen the metal-carbon interactions, thereby synergistically improving catalyst performance. When used as electrocatalysts for electrocatalytic CO_2 reduction, bismuth-, indium-, and tin/carbon-carrier-based catalysts exhibit excellent Faraday efficiencies of 92.8%, 86.4%, and 73.3%, respectively, for formate generation in flow cells. The influence of different metals and calcination temperatures on catalytic performance was examined to provide valuable insights into the rational design of carbon-based electrocatalysts with enhanced electrocatalytic activity.

1. Introduction

The urgent need to upgrade and transform energy structures has arisen from the global energy crisis and worsen environmental problems [1,2]. Therefore, the utilization of renewable energy sources and efficient energy conversion are pivotal in addressing these challenges [3,4]. With advancements in electrochemical catalysis technology, CO_2 can be electrically converted into high-value chemicals, enabling product selection through catalyst design and regulation. Additionally, this method enables the conversion of electricity generated by renewable energy sources to chemical energy, providing a promising strategy for addressing energy shortages and achieving carbon neutrality. However, limited by the high thermodynamic stability of CO_2 molecules, competitive hydrogen evolution reactions, and complexity of products, the selection and design of catalysts play crucial roles in effectively improving product selectivity and energy efficiency utilization [5-8].

Functional nanoparticles (NPs) dispersed on conductive carbon carriers offer significant benefits for enhancing the efficiency and selectivity of CO_2 reduction [9]. These conductive carriers not only enable efficient electron and heat transfer but also effectively disperse and stabilize NPs to prevent aggregation [10]. Currently, there are two common synthetic strategies for fabricating functional NPs dispersed on conductive carbon carriers: synthesis-assembly and top-down methods [11]. In the former approach, metal NPs are prepared using wet chemical methods, followed by impregnation and drying to combine them with carbon carriers. Although it allows for the effective regulation of nanoparticle size and phase composition, residues from ligands and surfactants influence the surface-active sites on the catalysts, lowering catalytic activity. Additionally, weak interactions between metal NPs and carriers hinder the catalyst stability, leading to the aggregation and redistribution of metal NPs [12,13]. On the other hand, the top-down synthesis strategy can facilitate strong interactions between metal carriers, but its limitations restrict the applicability. For instance, the design of precursors is relatively intricate, and the synthesis of MOF primarily involves hydrothermal and in situ pyrolysis processes. Simultaneously, the inevitable accumulation or volatilization of metal NPs during thermal decomposition results in the loss of active sites, reducing the activity of the catalyst [14-18].

In this study, polyaniline (PANI) impregnated with metal salts was used as the organic carbon carrier. Through rapid thermal shock treatment, a uniform dispersion of metal nanoparticles on a carbon substrate (M-PANI-T) was achieved. The short duration of thermal shock limits the migration of metal atoms, and defects on the carbon carrier generated by pyrolysis play a crucial role in effectively anchoring metal nanoparticles. Therefore, a series of carbon-based catalysts were prepared to investigate their electrocatalytic performance in carbon dioxide reduction reaction (CO_2RR). Different temperatures were adjusted by varying

---

ARTICLE IN PRESS

JID: CHPHMA
[m5GeSdc;June 27, 2024;18:25]

W. Guo, X. Cao, A. Zhou et al.
ChemPhysMater xxx (xxxx) xxx

the treatment time to further explore their impact on catalytic performance. Electrochemical analysis revealed that the Bi-PANI-2, In-PANI-3, and Sn-PANI-3 catalysts exhibited excellent Faraday efficiency (FE) for formate in flow cells. The combination of electrochemical and in situ characterization techniques further explored the influence of the metal active sites and calcination temperature on catalyst activity and revealed the reaction mechanism. This study provides a feasible approach for the rapid synthesis of efficient CO_2 reduction electrocatalysts.

2. Results and discussion

The carbon carrier PANI was prepared via oxidant-initiated aniline polymerization under acidic conditions (Fig. S1) [19]. PANI was then homogeneously mixed with a specific proportion of the metal salt in ethanol, and the solvent was evaporated to obtain the carbon-loaded metal salt precursors. Subsequently, a carbon-loaded metal nanoparticle catalyst was prepared using rapid thermal shock via Joule heating (Fig. 1(a)). Typically, a high temperature of 1100 °C could be reached within just 0.65 s (Fig. 1(b)). This universality was further investigated by changing the type of metal salt and the calcination temperature. This time-saving method restricts the migration of metal atoms owing to the rapid heating process over a short period, thereby inhibiting nanoparticle aggregation and improving the dispersion of active sites [20].

With an increase in thermal shock temperature, Raman spectroscopy analysis revealed that the degree of defects in the graphite peak grad-

ually increased, promoting the conductivity of the catalyst (Fig. 1(c)) [21]. Scanning electron microscopy (SEM) images demonstrate that the calcined PANI exhibited interconnected particles, enhancing the surface area for dispersing active sites on the carbon support (Fig. 1(d)). As shown in Figs. 1(g)–(e), Bi-PANI-2 exhibits a particle size distribution of 10–20 nm. However, Bi-PANI-1 predominantly consists of larger nanoparticles, possibly due to aggregation. During the high-temperature treatment, the size of indium and tin metal NPs increased (Figs. S2 and S3). With prolonged heat treatment, an increase in the migration time of metal atoms results in aggregation. Nevertheless, the size of the In-PANI-1 nanoparticles was maintained at approximately 25–50 nm even when subjected to the highest temperature. Thus, the NPs size can be changed by both the nature of the metal and the heating duration [22,23]. Different metals exhibit distinct dispersion states on carbon carriers due to their different boiling points. Moreover, the heating duration affected the activity of the catalysts by influencing the conductivity and aggregation state of the carbon carriers.

Transmission electron microscopy (TEM) images (Figs. 2(a)–(c)) reveal the uniform distribution of nanoparticles on the Bi-APNI-2 carbon. Similarly, In-PANI-3 and Sn-PANI-3 exhibit the coexistence of smaller NPs within the bulk structure, consistent with the SEM observations. High-resolution transmission electron microscopy (HRTEM) indicates uniform distributions of NPs with a small size of approximately 5 nm, further demonstrating that rapid thermal shock enabled the distribution of metal active sites (Figs. 2(d)–(f) and S4). Compared with traditional
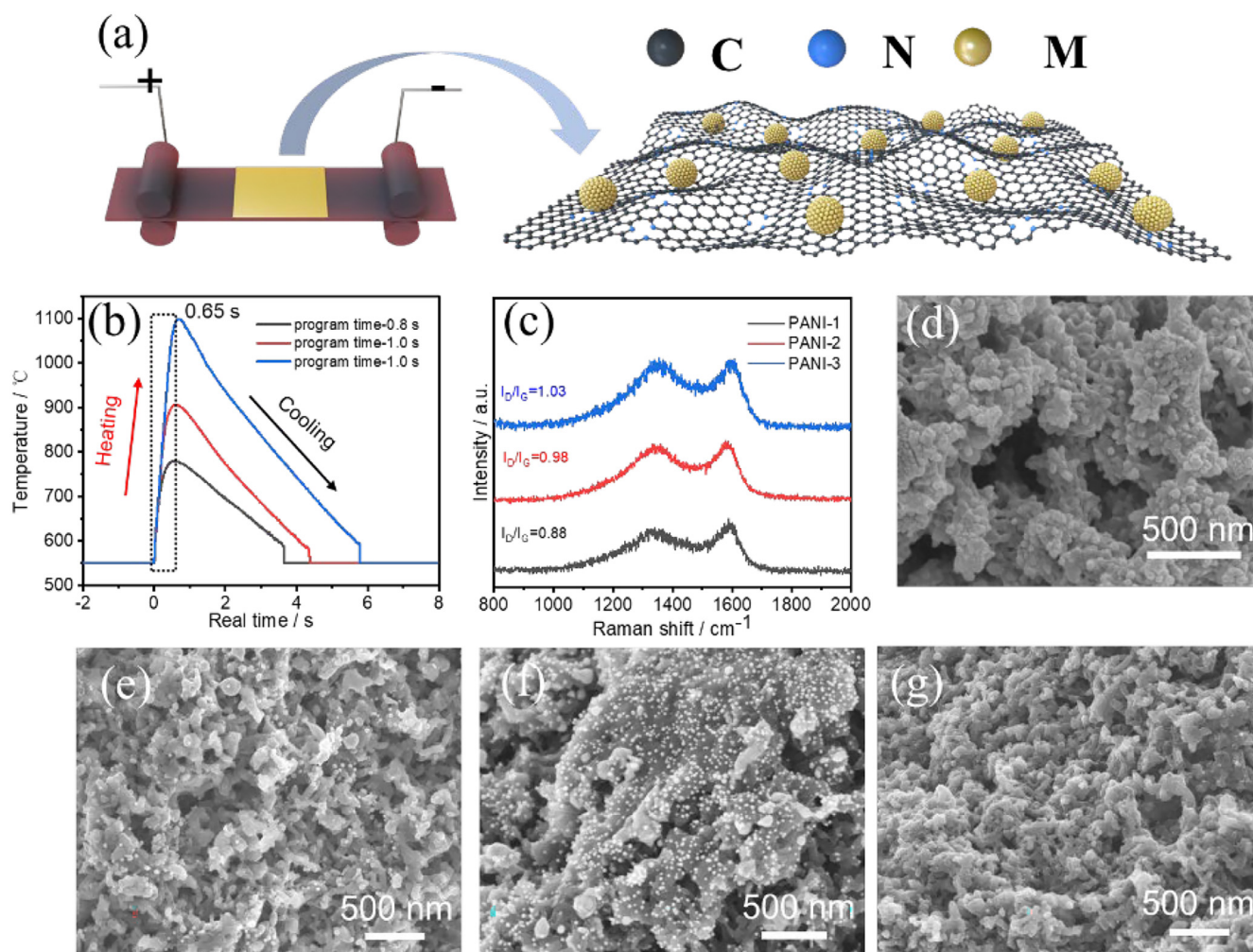

Fig. 1. (a) Scheme illustrating the synthesis process for M-PANI-T. (b) Temperature evolution during thermal shock. (c) Raman spectra of polyaniline (PANI) after thermal treatment at different temperatures. Scanning electron microscopy (SEM) images of (d) PANI-2, (e) Bi-PANI-1, (f) Bi-PANI-2, and (g) Bi-PANI-3.
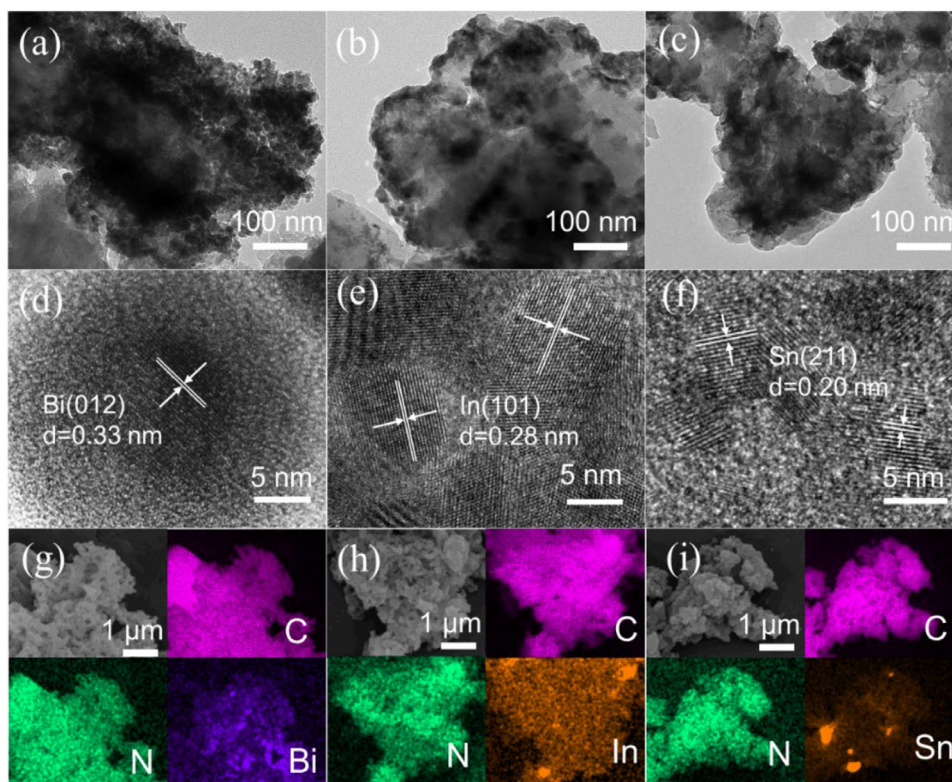
Fig. 2. (a)–(c) Transmission electron microscopy (TEM) images, (d)–(f) High-resolution transmission electron microscopy (HRTEM), and (g)–(i) Energy-dispersive X-ray spectroscopy (EDS) mapping of Bi-PANI-2, In-PANI-3, and Sn-PANI-3.

calcination, obvious aggregation of nanoparticles results in larger particle sizes of 50–500 nm (Fig. S5). The lattice spacing of 0.33 nm corresponds to the Bi (012) lattice, suggesting the formation of a metallic bismuth phase (Fig. 2(d)) [24]. Meanwhile, In-PANI-3 and Sn-PANI-3 display lattice spacings of 0.28 and 0.20 nm respectively, corresponding to In (101) and Sn (211) lattices, respectively (Figs. 2(e)(f)) [25,26]. These results demonstrate that carbon also functions as a reducing agent to convert metal salts into metal NPs during pyrolysis. The EDS mapping images confirm the homogeneous distribution of C and N with the corresponding metal elements. Nitrogen doping improves the electronic conductivity of the carbon matrix and regulates the electronic state of the local environment of the active site (Figs. 2(g)–(i)) [27].

The X-ray powder diffraction (XRD) patterns show that the bismuth, indium, and tin-based samples exhibit the phase of the standard metal peaks, indicating that the metal NPs function as active sites (Fig. 3(a)) [24-26]. As decipted in Fig. S6(a), the intensity of Bi metallic peak first increased and then decreased, contributed to enhanced crystallinity and volatilization of bismuth with gradual increase in temperature. For indium and tin metals with higher boiling points, the intensity change of the peaks was not significant (Figs. S6(b)(c)). The chemical composition of the catalyst surface was then analyzed by X-ray photoelectron spectroscopy (XPS) (Figs. S7–S9). The existence of C–N (285.7 eV), pyrrolic (400.4 eV), pyridinic (398.6 eV), and graphitic N (402.5 eV) was clearly observed in the analysis of the C 1s and N 1s peaks. Nitrogen doping enhances the electrical conductivity of the carbon matrix and effectively adsorbs specific cations through coordination principles, thus effectively promoting the dispersion of NPs on carbon materials (Figs. 3(b)(c)) [28,29]. From Fig. 4(d), Bi 4f is resolved into typical peaks for Bi^0 (162.6 and 157.4 eV) and Bi^{3+} (164.6 and 159.4 eV). Similarly, the peaks exhibited by indium and tin belong to Sn^{2+} (495.4 and 487.0 eV), Sn^0 (493.4 and 485.0 eV), and In^{3+} (453.0 and 445.5 eV), respectively. The noticeable oxidation peaks in the corresponding metallic spectra can be attributed to the oxidation of

the sample surface due to exposure to air, which is reduced during the CO_2RR [30-33].

The catalysts were initially evaluated in H-type electrolytic cells. As shown in Figs. S10(a)(d), Bi-PANI-2 demonstrated the highest current density and FEs ($FE_{C1(HCOOH+CO)}$ of 93.9% and FE_{HCOOH} of 90.1%), suggesting favorable selectivity towards formate production [34]. Similarly, indium and tin-based catalysts exhibited comparable performance, achieving maximum FE_{HCOOH} of 80.5% and 60.2% (Figs. S10(b)(c)), respectively, with a small amount of CO as a by-product [35]. As shown in Figs. 4(a)–(c), Bi-PANI-2 exhibited the optimal partial current density and FE for formate, highlighting the excellent electrocatalytic activity of bismuth metal in the CO_2RR. Comparing different heat treatment temperatures for the same series of catalysts reveals that the factors influencing catalytic activity are multifaceted. For instance, in the case of the Bi-PANI-T sample, the dispersion of catalytical active sites plays a dominant role; a better dispersion of NPs on the carbon support results in better electrocatalytic performance (Fig. S11). Despite an increase in NPs size with prolonged heat treatment time for the indium- and tin-based catalysts, they still exhibited favorable catalytic activity owing to the coexistence of ultrafine nanoparticles. Meanwhile, the increased graphitic defects on the carbon substrate at higher temperatures accelerate electron transfer and enhance catalytic performance [36]. For various electrocatalysts including cadmium, antimony, and copper (Figs. S12–S14), no discernible NPs were observed on the surface of Cd-PANI-T due to the rapid volatilization of cadmium with its low boiling point during the thermal shock process. Consequently, Cd-PANI-1 exhibited poor catalytic performance with a total FE for C_1 products of 48.2%, significantly lower than those of the bismuth-, indium-, and tin-based catalysts (Fig. S11(d)). In addition, Sb-PANI-T (Fig. S13) and Cu-PANI-T (Fig. S14) catalysts showed similar aggregation states but poorer catalytic activity compared to Sn-PANI-T catalysts [37,38].

A flow cell system equipped with a gas diffusion electrode was assembled to address the mass transfer limitation of CO_2 (Fig. 4(d)) [39],
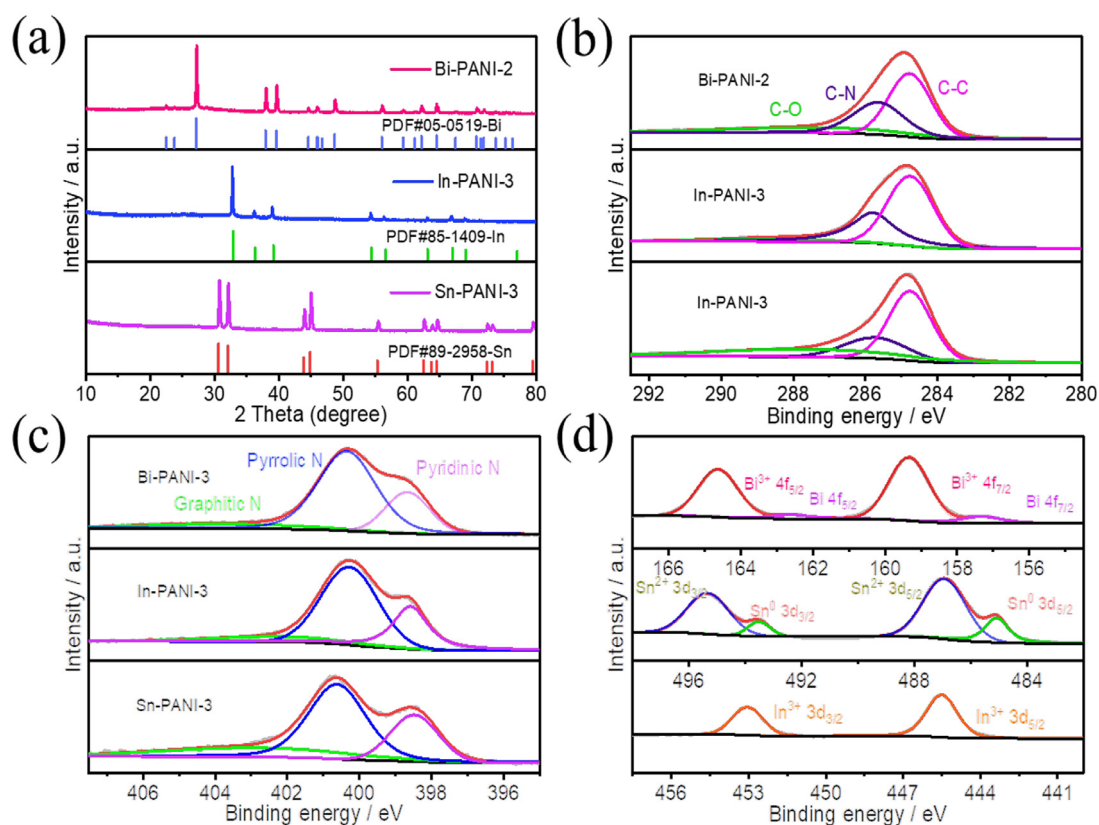
Fig. 3. (a) The X-ray powder diffraction (XRD) patterns and X-ray photoelectron spectroscopy (XPS) spectra of (b) C 1s, (c) N 1s, and (d) corresponding metallic spectra for Bi-PANI-2, In-PANI-3, and Sn-PANI-3.
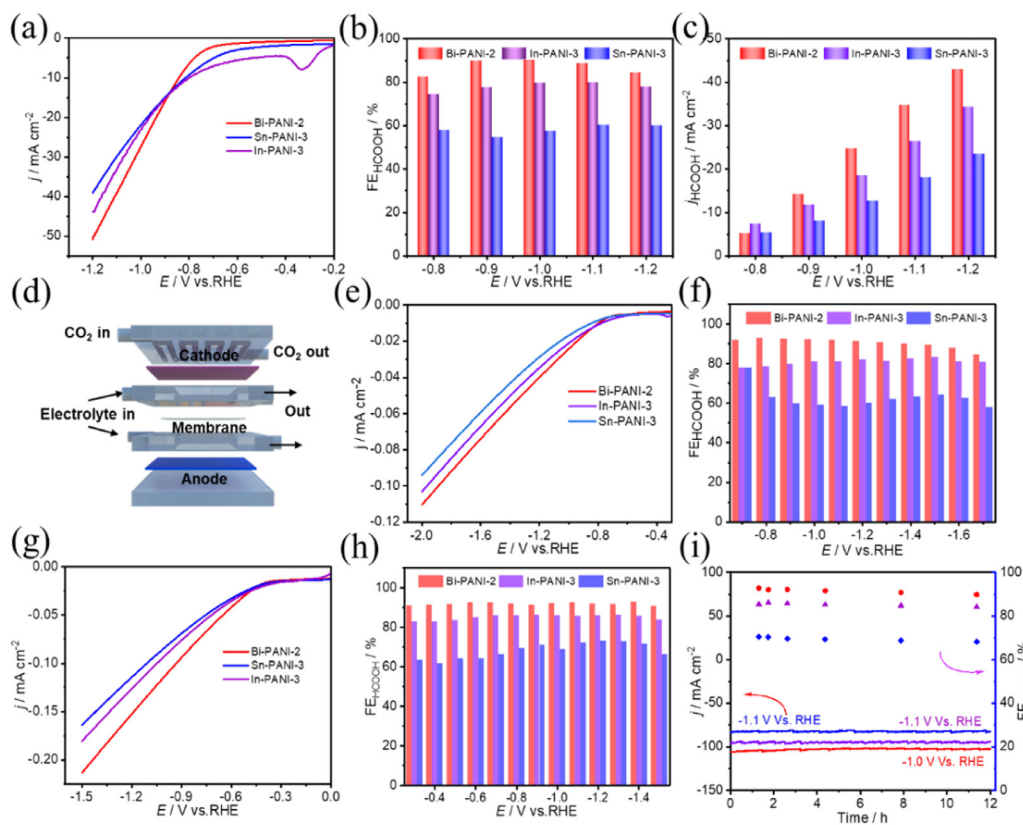

Fig. 4. The comparison of (a) linear sweep voltammetry (LSV), (b) Faraday efficiency (FE), and (c) partial current densities of formate for Bi-PANI-2, In-PANI-3, and Sn-PANI-3. (d) Schematic of the flow cell. (e)(g) LSVs and (f)(h) FEs in 1 M KHCO$_3$ and KOH for Bi-PANI-2, In-PANI-3, and Sn-PANI-3. (i) Stability tests and corresponding FEs for formate of the catalysts in 1 M KOH.
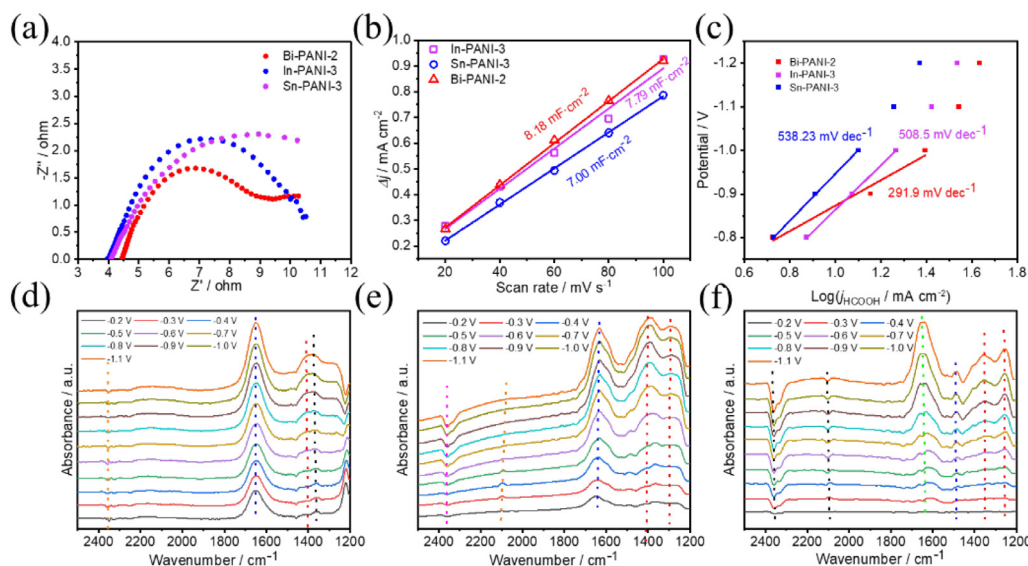
Fig. 5. (a) Electrochemical Impedance Spectroscopy (EIS), (b) C_{dl}, and (c) Tafel slope of Bi-PANI-2, In-PANI-3, and Sn-PANI-3. The in situ attenuated total reflection Fourier transform infrared spectroscopy (ATR-FTIR) spectra for (d) Bi-PANI-2, (e) In-PANI-3, and (f) Sn-PANI-3.

enabling direct contact between the catalyst and CO_2 gas, thus facilitating rapid mass transfer [40]. As shown in Figs. 4(e)(f), the implementation of the flow-cell system significantly improved the current density and FE of formate within a wider potential window. Specifically, Bi-PANI-2 exhibited the highest FE_{HCOOH} of 92.9% at −1.0 V vs. RHE, superior to In-PANI-3 (82.0%) and Sn-PANI-3 (78.1%). Moreover, when tested in 1 M KOH electrolyte, the current densities further increased to 113.4, 93.1, and 82.0 mA cm^{-2} for Bi-PANI-2, In-PANI-3, and Sn-PANI-3 catalysts at −1.0 V, respectively, which are approximately four times higher than those obtained from the H-type cell (Fig. 4(g)). The FE_{HCOOH} of Bi-PANI-2 and In-PANI-3 surpassed 90% and 80%, respectively, within the potential range from −0.3 to −1.5 V, achieving the highest FE values of 92.8% and 86.4%. Meanwhile, Sn-PANI-3 exhibited a significantly lower FE of 73.3% compared to the other two catalysts but was still higher than the FE in the 0.5 M and 1 M KHCO$_3$ electrolytes. Stability is also a crucial parameter for evaluating the performance of the catalyst. After 12 h, only a marginal decrease in the FE was observed, indicating the sustained high stability and activity of all three catalysts (Fig. 4(i)). Based on the SEM images obtained after the stability test (Fig. S15), no obvious aggregation was observed, further indicating good stability. A comprehensive analysis revealed that the anchoring of carbon defects, along with the Joule heating-induced dispersion processes, facilitated the dispersion of active sites, ultimately resulting in exceptional catalytic activity and stability.

The catalytic mechanism was further investigated through electrochemical tests and corresponding in situ characterization. The impedance spectra (Figs. 5(a) and S15) showed that Bi-PANI-2 exhibited the lowest charge transfer resistance, facilitating faster electron transfer, thus accelerating the reaction process and improving the catalytic activity [41]. Additionally, analysis of the double-layer capacitance (C_{dl}) revealed that the electrochemical activity surface area (ECSA) of the catalysts within the same series generally increased with higher heat treatment temperatures (Figs. S16 and S17). Combined with the BET adsorption-desorption isotherms, the specific surface area of PANI after carbonization reaches 307.08 m^2 g^{-1}, significantly higher than that of PANI (31.92 m^2 g^{-1}), which can be attributed to the defects induced exposure of surfaces (Fig. S18(a)). Additionally, pore size analysis and CO_2 adsorption isotherms indicated that the pyrolysis process led to a multistage pore structure in the carbon substrate, promoting mass transfer, enhancing CO_2 adsorption on the catalyst surface, and ultimately improving catalytic reaction activity (Figs. S18(b)(c)). Bi-PANI-2 exhibited an ideal active surface area due to the synergistic effects between

the carbon carrier and the dispersed active sites. However, the ECSA of Bi-PANI-3 decreased due to the loss of active sites (Figs. 5(b) and S19) [42]. Tafel slopes were obtained to investigate the kinetics of the CO_2RR, indicating that the rate-determining step of the reaction was the generation of a CO_2^{*-} intermediate (Fig. 5(c)) [43]. A lower Tafel slope suggested a faster rate of intermediate generation, facilitating protonation and thereby enhancing catalytic activity [44]. In situ ATR-FTIR was used to observe the reaction intermediates and elucidate the reaction mechanism. For the series of catalysts, distinct absorption peaks were observed at 2360 and 1640 cm^{-1} for CO_2 and H_2O, respectively [45]. The O–C–O vibration peak at 1415 cm^{-1} corresponds to two oxygen-bonded *OCHO species on the Bi-PANI-2 surface (Fig. 5(d)), indicating a rapid transformation process from CO_2^{*-} to *OCHO. Similar vibration peaks at 1405 and 1358 cm^{-1} were also observed for the In-PANI-3 (Fig. 5(e)) and Sn-PANI-3 (Fig. 5(f)) samples, confirming a favorable transformation pathway for formate formation [46,47]. Notably, both In-PANI-3 and Sn-PANI-3 showed prominent absorption peaks in the range of 2000–2100 cm^{-1} at lower potentials, indicating CO* generation during the CO formation process. The theoretical potential for CO generation was lower than that for HCOOH generation, implying the formation of CO by-products at lower potentials. As the potential gradually increased, formate production became dominant, leading to the gradual disappearance of the CO* peak and confirming the excellent catalytic performance of these catalysts.

3. Conclusions

In summary, a series of carbon-loaded nanoparticles (M-PANI-T) were synthesized using the Joule rapid thermal shock method, and their electrocatalytic performance was investigated. The rapid thermal shock treatment effectively minimized the aggregation of metal atoms and facilitated the uniform distribution of NPs on the carbon carrier by leveraging the anchoring effect of the defective carbon carriers. Electrochemical performance testing revealed that the bismuth, indium, and tin/carbon catalysts exhibited excellent Faraday efficiencies for formate in flow cells, with values of 92.8%, 86.4%, and 73.3%, respectively. This approach presents a viable strategy for the rapid synthesis of catalysts. Additionally, characterization revealed that the catalyst performance is influenced by both the active sites and the carbon carrier, rather than being solely dependent on individual factors, providing valuable theoretical insights for future catalyst design.

Declaration of Competing Interest

CRediT authorship contribution statement

Weijian Guo: Writing – original draft, Methodology, Investigation. **Xueying Cao:** Writing – original draft, Software, Investigation. **Ao Zhou:** Writing – original draft. **Wenwen Cai:** Writing – original draft, Methodology. **Jintao Zhang:** Writing – review & editing, Supervision.

Acknowledgements

Supplementary materials

Supplementary material associated with this article can be found, in the online version, at doi:10.1016/j.chphma.2024.06.002.

References

[1] L. Li, X. Li, Y. Sun, Y. Xie, Rational design of electrocatalytic carbon dioxide reduction for a zero-carbon network, Chem. Soc. Rev. 51 (2022) 1234–1252, doi:10.1039/d1cs00893e.

[2] A. Nairan, Z. Feng, R. Zheng, U. Khan, J. Gao, Engineering metallic alloy electrode for robust and active water electrocatalysis with large current density exceeding 2000 mA cm^{-2}, Adv. Mater. (2024) e2401448, doi:10.1002/adma.202401448.

[3] P. Sun, S. Liu, X. Zheng, G. Hu, Q. Zhang, X. Liu, G. Zheng, Y. Chen, Challenges and opportunities of atomic-scales reactive sites in thriving electrochemical CO$_2$ reduction reaction, Nano Today 55 (2024) 102152, doi:10.1016/j.nantod.2024.102152.

[4] Waris Chaudhary M.S., A.H. Anwer, S. Sultana, P.P. Ingole, S.A.A. Nami, M.Z. Khan, A review on development of carbon-based nanomaterials for energy storage devices: Opportunities and challenges, Ener. Fuels 37 (2023) 19433–19460, doi:10.1021/acs.energyfuels.3c03213.

[5] G. Wang, J. Chen, Y. Ding, P. Cai, L. Yi, Y. Li, C. Tu, Y. Hou, Z. Wen, L. Dai, Electrocatalysis for CO$_2$ conversion: From fundamentals to value-added products, Chem. Soc. Rev. 50 (2021) 4993–5061, doi:10.1039/D0CS00071J.

[6] S.A. Farooqi, A.S. Farooqi, S. Sajjad, C. Yan, A.B. Victor, Electrochemical reduction of carbon dioxide into valuable chemicals: A review, Environ. Chem. Lett. 21 (2023) 1515–1553, doi:10.1007/s10311-023-01565-7.

[7] M. Schreier, F. Héroguel, L. Steier, S. Ahmad, J.S. Luterbacher, M.T. Mayer, J. Luo, M. Grätzel, Solar conversion of CO$_2$ to CO using earth-abundant electrocatalysts prepared by atomic layer modification of CuO, Nat. Ener. 2 (2017) 17087, doi:10.1038/nenergy.2017.87.

[8] Y.J. Zhang, V. Sethuraman, R. Michalsky, A.A. Peterson, Competition between CO$_2$ reduction and H$_2$ evolution on transition-metal electrocatalysts, ACS Catal. 4 (2014) 3742–3748, doi:10.1021/cs5012298.

[9] D. Wang, L. Zhu, J.F. Chen, L. Dai, Liquid marbles based on magnetic upconversion nanoparticles as magnetically and optically responsive miniature reactors for photocatalysis and photodynamic therapy, Angew. Chem. Int. Ed. 55 (2016) 10795–10799, doi:10.1002/anie.201604781.

[10] Y. Yao, F. Chen, A. Nie, S.D. Lacey, R.J. Jacob, S. Xu, Z. Huang, K. Fu, J. Dai, L. Salamanca-Riba, M.R. Zachariah, R. Shahbazian-Yassar, L. Hu, In situ high temperature synthesis of single-component metallic nanoparticles, ACS Cent. Sci. 3 (2017) 294–301, doi:10.1021/acscentsci.6b00374.

[11] Z. Chen, X. Zeng, S. Wang, A. Cheng, Y. Zhang, Advanced carbon-based nanocatalysts and their application in catalytic conversion of renewable platform molecules, ChemSusChem 15 (2022) e202200411, doi:10.1002/cssc.202200411.

[12] Z. Fan, H. Zhang, Crystal phase-controlled synthesis, properties and applications of noble metal nanomaterials, Chem. Soc. Rev. 45 (2016) 63–82, doi:10.1039/C5CS00467E.

[13] K.D. Gilroy, A. Ruditskiy, H.C. Peng, D. Qin, Y. Xia, Bimetallic nanocrystals: Syntheses, properties, and applications, Chem. Rev. 116 (2016) 10414–10472, doi:10.1021/acs.chemrev.6b00211.

[14] K. Yamamoto, T. Imaoka, W.J. Chun, O. Enoki, H. Katoh, M. Takenaga, A. Sonoi, Size-specific catalytic activity of platinum clusters enhances oxygen reduction reactions, Nat. Chem. 1 (2009) 397–402, doi:10.1038/nchem.288.

[15] S. Bonanni, K. Aït-Mansour, W. Harbich, H. Brune, Reaction-induced cluster ripening and initial size-dependent reaction rates for CO oxidation on Pt$_n$/TiO$_2$ (110)-(1×1), J. Am. Chem. Soc. 136 (2014) 8702–8707, doi:10.1021/ja502867r.

[16] A. Wong, Q. Liu, S. Griffin, A. Nicholls, J.R. Regalbuto, Synthesis of ultrasmall, homogeneously alloyed, bimetallic nanoparticles on silica supports, Science 358 (2017) 1427–1430, doi:10.1126/science.aao6538.

[17] J. Feng, L. Chen, P. Song, X. Wu, A. Wang, J. Yuan, Bimetallic AuPd nanoclusters supported on graphitic carbon nitride: One-pot synthesis and enhanced electrocatalysis for oxygen reduction and hydrogen evolution, Int. J. Hydro. Ener. 41 (2016) 8839–8846, doi:10.1016/j.ijhydene.2016.03.108.

[18] Y. Wang, J. Ma, X. Cao, S. Chen, L. Dai, J. Zhang, Bionic mineralization toward scalable MOF films for ampere-level biomass upgrading, J. Am. Chem. Soc. 145 (2023) 20624–20633, doi:10.1021/jacs.3c07790.

[19] A. Singh, R. Kale, A. Sarkar, V. Juvekar, A. Contractor, Autogenous oxidation/reduction of polyaniline in aqueous sulfuric acid, Processes 10 (2022) 443, doi:10.3390/pr10030443.

[20] Y. Yao, Z. Huang, P. Xie, T. Li, S.D. Lacey, M. Jiao, H. Xie, K.K. Fu, R.J. Jacob, D.J. Kline, Y. Yang, M.R. Zachariah, C. Wang, R. Shahbazi-Yassar, L. Hu, Ultrafast, controllable synthesis of sub-nano metallic clusters through defect engineering, ACS Appl. Mater. Interf. 11 (2019) 29773–29779, doi:10.1021/acsami.9b07198.

[21] H. Zhuang, T. Zhang, H. Xiao, F. Zhang, P. Han, H. Gu, J. Jiao, W. Chen, Q. Gao, Free-standing cross-linked hollow carbonaceous nanovesicle fibers with atomically dispersed CoN$_4$ electrocatalytic centers driving high-performance Li-S battery, Appl. Catal. B-Environ. 340 (2024) 123273, doi:10.1016/j.apcatb.2023.123273.

[22] W. Jung, H. Park, J. Jang, D.Y. Kim, D.W. Kim, E. Lim, J.Y. Kim, S. Choi, J. Suk, Y. Kang, I.D. Kim, J. Kim, M. Wu, H. Jung, Polyelemental nanoparticles as catalysts for a Li–O$_2$ battery, ACS Nano 15 (2021) 4235–4244, doi:10.1021/acsnano.0c06528.

[23] Y. Yao, Z. Huang, P. Xie, L. Wu, L. Ma, T. Li, Z. Pang, M. Jiao, Z. Liang, J. Gao, Y. He, D.J. Kline, M.R. Zachariah, C. Wang, J. Lu, T. Wu, T. Li, C. Wang, R. Shahbazian-Yassar, L. Hu, High temperature shockwave stabilized single atoms, Nat. Nanotechnol 14 (2019) 851–857, doi:10.1038/s41565-019-0518-7.

[24] J. Yang, J. Xian, Q. Liu, Y. Sun, G. Li, Bi nanoparticles in situ encapsulated by carbon film as high-performance anode materials for Li-ion batteries, J. Energy. Chem. 69 (2022) 524–530, doi:10.1016/j.jechem.2022.01.026.

[25] X. Cao, B. Wulan, Y. Wang, J. Ma, S. Hou, J. Zhang, Atomic bismuth induced ensemble sites with indium towards highly efficient and stable electrocatalytic reduction of carbon dioxide, Sci. Bull. 68 (2023) 1008–1016, doi:10.1016/j.scib.2023.04.026.

[26] Z. Liu, C. Liu, S. Mao, X. Huang, Heterogeneous structure of Sn/SnO$_2$ constructed via phase engineering for efficient and stable CO$_2$ reduction, ACS Appl. Mater. Interf. 15 (2023) 7529–7537, doi:10.1021/acsami.2c18522.

[27] K. Zhou, S. Wang, X. Guo, G. Zhong, Z. Liu, M. Huang, Y. Bao, D. Han, L. Niu, Bismuth nanoparticles encapsulated in nitrogen-rich porous carbon nanofibers as a high-performance anode for aqueous alkaline rechargeable batteries, Small 18 (2022) e2105770, doi:10.1002/smll.202105770.

[28] Z. Li, C. Zhang, J. Bu, L. Zhang, L. Cheng, M. Wu, Constructing a novel carbon skeleton to anchor Sn/SnO$_2$ nanodots for flexible supercapacitor with excellent rate capability, Carb. N Y 194 (2022) 197–206, doi:10.1016/j.carbon.2022.03.079.

[29] S. Yang, S. Xu, J. Tong, D. Ding, G. Wang, R. Chen, P. Jin, X.C. Wang, Overlooked role of nitrogen dopant in carbon catalysts for peroxymonosulfate activation: Intrinsic defects or extrinsic defects? Appl. Catal. B-Environ. 295 (2021) 120291, doi:10.1016/j.apcatb.2021.120291.

[30] J. Yang, X. Wang, Y. Qu, X. Wang, H. Huo, Q. Fan, J. Wang, L.M. Yang, Y. Wu, Bi-based metal-organic framework derived leafy bismuth nanosheets for carbon dioxide electroreduction, Adv. Ener. Mater. 10 (2020) 2001709, doi:10.1002/aenm.202001709.

[31] S.H. Li, S. Hu, H. Liu, J. Liu, X. Kang, S. Ge, Z. Zhang, Q. Yu, B. Liu, Two-dimensional metal coordination polymer derived Indium nanosheet foreefficient carbon dioxidereduction to formate, ACS Nano 17 (2023) 9338–9346, doi:10.1021/acsnano.3c01059.

[32] S. Gao, N. Wang, S. Li, D. Li, Z. Cui, G. Yue, J. Liu, X. Zhao, L. Jiang, Y. Zhao, A multi-wall Sn/SnO$_2$@carbon hollow nanofiber anode material for high-rate and long-life lithium-ion batteries, Angew. Chem. Int. Ed. 59 (2020) 2465–2472, doi:10.1002/anie.201913170.

[33] P. Deng, H. Wang, R. Qi, J. Zhu, S. Chen, F. Yang, L. Zhou, K. Qi, H. Liu, B.Y. Xia, Bismuth oxides with enhanced bismuth–oxygen structure for efficient electrochemical reduction of carbon dioxide to formate, ACS Catal. 10 (2019) 743–750, doi:10.1021/acscatal.9b04043.

[34] B. Wulan, L.L. Zhao, D.X. Tan, X.Y. Cao, J.Z. Ma, J.T. Zhang, Electrochemically driven interfacial transformation for high-performing solar-to-fuel electrocatalytic conversion, Adv. Ener. Mater. 12 (2022) 2103960, doi:10.1002/aenm.202103960.

[35] Y. Zhang, F. Li, J. Dong, K. Jia, T. Sun, L. Xu, Recent advances in designing efficient electrocatalysts for electrochemical carbon dioxide reduction to formic acid/formate, J. Electroana. Chem. 928 (2023) 117018, doi:10.1016/j.jelechem.2022.117018.

[36] W.b. Li, C. Yu, X.Y. Tan, S. Cui, Y.F. Zhang, J.S. Qiu, Recent advances in the electroreduction of carbon dioxide to formic acid over carbon-based materials, New Carb. Mater. 37 (2022) 277–287, doi:10.1016/s1872-5805(22)60592-4.

[37] W. Xie, T. Yang, N. Tian, X.H. Liu, J. Chen, Cu nanoparticles decorating N-doped erythrocyte-shaped carbon nanostructures for electrochemical CO$_2$ reduction, Ener. Fuels 36 (2022) 958–964, doi:10.1021/acs.energyfuels.1c03823.

[38] Q. Yang, J. Zhou, G. Zhang, C. Guo, M. Li, Y. Zhu, Y. Qian, Sb nanoparticles uniformly dispersed in 1-D N-doped porous carbon as anodes for Li-ion and Na-ion batteries, J. Mater. Chem. A 5 (2017) 12144–12148, doi:10.1039/C7TA03060F.

[39] P. Deng, F. Yang, Z. Wang, S. Chen, Y. Zhou, S. Zaman, B.Y. Xia, Metal-organic framework-derived carbon nanorods encapsulating bismuth oxides for rapid and

selective CO_2 electroreduction to formate, Angew. Chem. Int. Ed. 59 (2020) 10807–10813, doi:10.1002/anie.202000657.

[40] H. Jiang, R. Luo, Y. Li, W. Chen, Recent advances in solid-liquid-gas three-phase interfaces in electrocatalysis for energy conversion and storage, EcoMat 4 (2022) 12199, doi:10.1002/eom2.12199.

[41] Y. Duan, K. Liu, Q. Zhang, J. Yan, Q. Jiang, Efficient CO_2 reduction to HCOOH with high selectivity and energy efficiency over Bi/rGO catalyst, Small Methods 4 (2020) 1900846, doi:10.1002/smtd.201900846.

[42] C.C.L. McCrory, S. Jung, I.M. Ferrer, S.M. Chatman, J.C. Peters, T.F. Jaramillo, Benchmarking hydrogen evolving reaction and oxygen evolving reaction electrocatalysts for solar water splitting devices, J. Am. Chem. Soc. 137 (2015) 4347–4357, doi:10.1021/ja510442p.

[43] Y. Qiao, W. Lai, K. Huang, T. Yu, Q. Wang, L. Gao, Z. Yang, Z. Ma, T. Sun, M. Liu, C. Lian, H. Huang, Engineering the local microenvironment over Bi nanosheets for

highly selective electrocatalytic conversion of CO_2 to HCOOH in strong acid, ACS Catal. 12 (2022) 2357–2364, doi:10.1021/acscatal.1c05135.

[44] B. Wulan, X. Cao, D. Tan, J. Ma, J. Zhang, To stabilize oxygen on In/In_2O_3 heterostructure via Joule heating for efficient electrocatalytic CO_2 reduction, Adv. Funct. Mater. 33 (2023) 2209114, doi:10.1002/adfm.202209114.

[45] X. Cao, Y. Wang, D. Tan, B. Wulan, J. Ma, W. Guo, J. Zhang, Stepwise dispersion of nickel species for efficient coupling of electrocatalytic redox reactions, Chem. Eng. J. 454 (2023) 140062, doi:10.1016/j.cej.2022.140062.

[46] W. Wang, X. Wang, Z. Ma, Y. Wang, Z. Yang, J. Zhu, L. Lv, H. Ning, N. Tsubaki, M. Wu, Carburized In_2O_3 nanorods endow CO_2 electroreduction to formate at 1 A cm^{-2}, ACS Catal. 13 (2023) 796–802, doi:10.1021/acscatal.2c05006.

[47] X. Cao, Y. Tian, J. Ma, W. Guo, W. Cai, J. Zhang, Strong p-d orbital hybridization on bismuth nanosheets for high performing CO_2 electroreduction, Adv. Mater. 36 (2024) 2309648, doi:10.1002/adma.202309648.